An efficient Eulerian finite element method for the shallow water equations

Emmanuel Hanert [a,b], Daniel Y. Le Roux [c], Vincent Legat [b] and Eric Deleersnijder [a]

[a] *Institut d'Astronomie et de Géophysique G. Lemaître, Université Catholique de Louvain, 2 Chemin du Cyclotron, B-1348 Louvain-la-Neuve, Belgium*

[b] *Centre for Systems Engineering and Applied Mechanics, Université Catholique de Louvain, 4 Avenue Georges Lemaître, B-1348 Louvain-la-Neuve, Belgium*

[c] *Département de Mathématiques et de Statistique, Université Laval, Québec, QC, G1K 7P4, Canada*

Abstract

The accuracy and efficiency of an Eulerian method is assessed by solving the nonlinear shallow water equations and compared with the performances of an existing semi-Lagrangian method. Both methods use a linear non-conforming finite element discretization for velocity and a linear conforming finite element discretization for surface elevation. This finite element pair is known to be computationally efficient and free of pressure modes. The model equations are carefully derived and a comparison is performed by simulating the propagation of slow Rossby waves in the Gulf of Mexico. Simulations show that the Eulerian model performs well and gives results comparable to high order semi-Lagrangian schemes using kriging interpolators.

Key words: finite elements, Euleurian, semi-Lagrangian, shallow water equations, Rossby waves, non-conforming linear interpolation, kriging

---

1 Introduction

The ocean circulation may be represented as the interaction of many different physical processes in a domain of complex shape. Those interactions are often nonlinear and spatially localized. As a consequence, a numerical model of the world ocean should be able to deal with nonlinearities, irregular geometries and localized phenomena.

Unstructured grids permit to accurately represent complex domains. Their flexibility also allows to achieve high resolution in regions of interest thanks to

Preprint submitted to Elsevier Science *16th August 2004*

suitable grid refinements. In the last years an increased interest has been paid toward ocean or coastal models using unstructured meshes. For those models, the spatial discretization is based either on finite elements (e.g. Le Provost et al., 1994; Myers and Weaver, 1995; Lynch et al., 1996; Le Roux et al., 2000; Legrand et al., 2001; Hanert et al., 2003; Nechaev et al., 2003; Danilov et al., 2004), spectral elements (e.g. Iskandarani et al., 1995, 2003) or finite volumes (Casulli and Walters, 2000; Chen et al., 2003).

The numerical treatment of nonlinear advection terms in the mass and momentum equations can be done either with an Eulerian, a Lagrangian or a semi-Lagrangian scheme. In Eulerian schemes, the evolution of the system is monitored from fixed positions in space. As a consequence, those methods are easy to implement as all the variables are computed at fixed grid points in the domain. However, their accuracy is often not so high as Lagrangian methods where the information is integrated along characteristics. Eulerian methods are used in most ocean circulation models. In Lagrangian schemes, the evolution of the system is monitored from fluid parcels that move with the flow. Such schemes often allow much larger time steps than Eulerian schemes. Their main disadvantage is that the distribution of fluid parcels can quickly become highly nonuniform which can render the scheme inaccurate. Such a problem can be circumvented by using semi-Lagrangian schemes. The idea behind those schemes is to choose a completely new set of parcels at every time step. This set of parcels is chosen such that they arrive exactly on the nodes of a regularly spaced mesh at the end of each time step. This method has proved to work particularly well in atmosphere modelling, especially when combined with a semi-implicit scheme (Robert, 1981, 1982; Robert et al., 1985). An extensive review of the applications of semi-Lagrangian methods to atmospheric problems is provided by Staniforth and Côté (1990). In ocean modelling, Behrens (1998) and Le Roux et al. (2000) showed that the combination of semi-Lagrangian schemes and finite elements could be an interesting approach.

In the present study, we compare an Eulerian and a semi-Lagrangian finite-element shallow water model to assess both approaches in the context of ocean modelling. Both models use a linear non-conforming approximation for velocity and a linear conforming approximation for elevation. Such a finite element pair is denoted $P_1^{NC} - P_1$. Non-conforming finite elements have been introduced by Crouzeix and Raviart (1973) to solve Stokes equations. They have proved to be well suited to represent transport processes thanks to an important flexibility and the ability to allow upwind weighed formulations (Hanert et al., 2004). The combination of linear conforming and non-conforming finite elements has first been studied by Hua and Thomasset (1984) to solve the shallow water equations. They showed that this finite element pair is computationally efficient and properly models the dispersion of the inertia-gravity waves. Le Roux (2003) performed a dispersion analysis and showed that the discrete frequency was monotonic for all resolutions.

The paper is organized as follows. We first present the model equations and the finite element discretization in sections 2 and 3 respectively. The $P_1^{NC} - P_1$ finite element pair is described in section 4. The Eulerian and semi-Lagrangian schemes are derived in sections 5 and 6 respectively. Section 7 presents the numerical experiments and a discussion of the methods performances. Conclusions are given in section 8.

2 Governing equations

We consider the following formulation of the shallow water problem: Let Ω be the two-dimensional model domain, we seek the velocity $\mathbf{u}(\mathbf{x}, t)$ and the surface elevation $\eta(\mathbf{x}, t)$ which are solutions of the following equations:

$$\frac{\partial \eta}{\partial t} + \boldsymbol{\nabla} \cdot [(h + \eta)\mathbf{u}] = 0, \tag{1}$$

$$\frac{\partial \mathbf{u}}{\partial t} + \mathbf{u} \cdot \boldsymbol{\nabla} \mathbf{u} + f\mathbf{k} \times \mathbf{u} = -g\boldsymbol{\nabla}\eta, \tag{2}$$

where h is the reference depth of the fluid, f is the Coriolis parameter, $\mathbf{k}$ is a unit vector in the vertical direction, g is the gravitational acceleration, $\boldsymbol{\nabla}$ is the two-dimensional gradient operator.

Another form of equations (1) and (2) can be obtained by introducing total derivatives and writing the mass equation in terms of the logarithm of $h + \eta$:

$$\frac{D \ln(h + \eta)}{Dt} + \boldsymbol{\nabla} \cdot \mathbf{u} = 0, \tag{3}$$

$$\frac{D\mathbf{u}}{Dt} + f\mathbf{k} \times \mathbf{u} = -g\boldsymbol{\nabla}\eta, \tag{4}$$

where $D/Dt = \partial/\partial t + \mathbf{u} \cdot \boldsymbol{\nabla}$ denotes the total or Lagrangian derivative. Equations (3) and (4) will be used to derive the semi-Lagrangian scheme. Obviously, the two sets of equations are strictly equivalent in the continuous limit, while in the numerical or discrete limit, they are no longer equivalents.

The selection of the logarithmic form of the mass equation follows the approach of Le Roux et al. (2000). Such a formulation of the continuity equation may not appear obvious. First of all, the logarithmic term may be problematic as it cannot be computed exactly in a numerical scheme. The resulting semi-Lagrangian scheme is then likely to be non-conservative. The same conservation issue arises from the interpolation procedures that are also generally non-conservative. Therefore, the conservation has to be explicitely enforced at each time step by adding a constant elevation correction to the computed elevation field. This is a classical way to proceed even if other strategies exist to deliver conservative semi-Lagrangian schemes. The interest of the logarithmic form of the mass equation is to get a linear divergence term at the prize of a linearization of the logaritm. Other forms could also be selected (e.g. Behrens, 1998) but will not be analyzed here.

For both sets of equations, the solution is specified by imposing no normal flow boundary conditions ($\mathbf{u} \cdot \mathbf{n} = 0$ on $\partial\Omega$) and initial conditions.

3 Finite element spatial discretization

Let $\mathcal{P}$ be a partition of the domain Ω into N_E disjoint open elements Ω_e:

$$\bar{\Omega} = \bigcup_{e=1}^{N_E} \bar{\Omega}_e \quad \text{and} \quad \Omega_e \cap \Omega_f = \emptyset \quad \text{for } e \neq f,$$

where $\bar{\Omega}$ is the closure of Ω. Each element Ω_e has a boundary $\partial\Omega_e$ and the outward unit normal to $\partial\Omega_e$ is $\mathbf{n}_e$. Let Γ be the ensemble of interelement boundaries $\Gamma_l = \partial\Omega_e \cap \partial\Omega_f$ with $e > f$ inside the domain, with all possible combinations:

$$\bar{\Gamma} = \bigcup_{l=1}^{N_\Gamma} \bar{\Gamma}_l \quad \text{and} \quad \Gamma_l \cap \Gamma_m = \emptyset \quad \text{for } l \neq m,$$

where N_Γ is the number of elements in Γ. Each $\Gamma_l \in \Gamma$ is associated with a unique unit normal vector $\mathbf{n}$ which points from Ω_e to Ω_f. In this paper, $\mathcal{P}$ will be a triangulation of non-overlapping triangles. The total number of vertices and segments in the triangulation are denoted N_V and N_S.

The variational or weak formulation of equations (1) and (2) is built in such a way that the solution for elevation is continous everywhere whereas the solution for velocity can be discontinuous between the elements Ω_e. It requires continuity constraints on the solution values and reads:

Find $\eta(\mathbf{x}, t) \in \mathcal{E}$ and $\mathbf{u}(\mathbf{x}, t) \in \mathcal{U}$ such that

$$\sum_{e=1}^{N_E} \int_{\Omega_e} \left(\frac{\partial \eta}{\partial t} \hat{\eta} - (h + \eta) \mathbf{u} \cdot \boldsymbol{\nabla} \hat{\eta} \right) \, \mathrm{d}\Omega$$

$$+\sum_{e=1}^{N_E}\int_{\partial\Omega_e}(h+\eta)\hat{\eta}\mathbf{u}\cdot\mathbf{n}_e\,\mathrm{d}\Gamma = 0 \quad \forall\hat{\eta}\in\mathcal{E}, \tag{5}$$

$$\sum_{e=1}^{N_E}\int_{\Omega_e}\left(\frac{\partial\mathbf{u}}{\partial t}\cdot\hat{\mathbf{u}} - (\boldsymbol{\nabla}\cdot(\mathbf{u}\hat{\mathbf{u}}))\cdot\mathbf{u} + f(\mathbf{k}\times\mathbf{u})\cdot\hat{\mathbf{u}} + g\boldsymbol{\nabla}\eta\cdot\hat{\mathbf{u}}\right)\mathrm{d}\Omega$$

$$+\sum_{e=1}^{N_E}\int_{\partial\Omega_e}(\mathbf{u}\mathbf{u}\cdot\mathbf{n}_e)\cdot\hat{\mathbf{u}}\,\mathrm{d}\Gamma$$

$$+\sum_{l=1}^{N_\Gamma}\int_{\Gamma_l}[\mathbf{u}]\cdot[\mathbf{a}(\hat{\mathbf{u}})]\,\mathrm{d}\Gamma = 0 \quad \forall\hat{\mathbf{u}}\in\mathcal{U}, \tag{6}$$

where $[\mathbf{s}] = \mathbf{s}_{|\Omega_e} - \mathbf{s}_{|\Omega_f}$ is the jump of $\mathbf{s}$ on an interior edge Γ_l, $\mathbf{s}_{|\Omega_e}$ denotes the restriction of $\mathbf{s}$ on Ω_e, and $\mathcal{E}$ and $\mathcal{U}$ are suitable functional spaces. The test functions $\hat{\eta}$ and $\hat{\mathbf{u}}$ belong to $\mathcal{E}$ and $\mathcal{U}$ respectively. The last integral in (6) is a continuity constraint that weakly imposes the continuity of the velocity between elements. The function $\mathbf{a}$ has to be selected to balance the continuity requirement versus the fulfilment of the differential equations in the weak formulation. It reads:

$$\mathbf{a}(\hat{\mathbf{u}}) = \begin{cases}\mathbf{u}\cdot\mathbf{n}(\lambda-1/2)\hat{\mathbf{u}} & \text{on } \Omega_e,\\ \mathbf{u}\cdot\mathbf{n}(\lambda+1/2)\hat{\mathbf{u}} & \text{on } \Omega_f,\end{cases}$$

where $\lambda\in[-1/2,1/2]$. Centered and upwind momentum advection schemes are obtained by choosing $\lambda=0$ and $\lambda=\frac{1}{2}\mathrm{sign}(\mathbf{u}(\mathbf{x})\cdot\mathbf{n}(\mathbf{x}))$ respectively. In the following, we will use the upwind parametrization that is usually selected (Houston et al., 2000; Hanert et al., 2004).

With this choice for the weight function and some standard algebra (Houston et al., 2000; Hanert et al., 2004), the variational formulation may be rewritten as:

Find $\eta(\mathbf{x},t)\in\mathcal{E}$ and $\mathbf{u}(\mathbf{x},t)\in\mathcal{U}$ such that

$$\sum_{e=1}^{N_E}\int_{\Omega_e}\left(\frac{\partial\eta}{\partial t}\hat{\eta} - (h+\eta)\mathbf{u}\cdot\boldsymbol{\nabla}\hat{\eta}\right)\mathrm{d}\Omega$$

$$+\sum_{l=1}^{N_\Gamma}\int_{\Gamma_l}\Big(\langle(h+\eta)\mathbf{u}\cdot\mathbf{n}\rangle[\hat{\eta}] + [(h+\eta)\mathbf{u}\cdot\mathbf{n}]\langle\hat{\eta}\rangle\Big)\,\mathrm{d}\Gamma = 0 \quad \forall\hat{\eta}\in\mathcal{E}, \tag{7}$$

$$\sum_{e=1}^{N_E}\int_{\Omega_e}\left(\frac{\partial\mathbf{u}}{\partial t}\cdot\hat{\mathbf{u}} - (\boldsymbol{\nabla}\cdot(\mathbf{u}\hat{\mathbf{u}}))\cdot\mathbf{u} + f(\mathbf{k}\times\mathbf{u})\cdot\hat{\mathbf{u}} + g\boldsymbol{\nabla}\eta\cdot\hat{\mathbf{u}}\right)\mathrm{d}\Omega$$

$$+\sum_{l=1}^{N_\Gamma}\int_{\Gamma_l}\langle\mathbf{u}\mathbf{u}\cdot\mathbf{n}\rangle_\lambda\cdot[\hat{\mathbf{u}}]\ \mathrm{d}\Gamma=0\quad\forall\hat{\mathbf{u}}\in\mathcal{U},\tag{8}$$

where $\langle\mathbf{s}\rangle$ and $\langle\mathbf{s}\rangle_\lambda$ denote the average and weighed average of $\mathbf{s}$ on the segment Γ_l respectively, with:

$$\begin{aligned}\langle\mathbf{s}\rangle&=\frac{1}{2}(\mathbf{s}_{|\Omega_e}+\mathbf{s}_{|\Omega_f})\\ \langle\mathbf{s}\rangle_\lambda&=(1/2+\lambda)\mathbf{s}_{|\Omega_e}+(1/2-\lambda)\mathbf{s}_{|\Omega_f}.\end{aligned}$$

A finite element approximation to the exact solution of equations (1) and (2) is found by replacing η and $\mathbf{u}$ with finite element approximations η^h and $\mathbf{u}^h$ in (7) and (8). Those approximations respectively belong to finite dimensional spaces $\mathcal{E}^h\subset\mathcal{E}$ and $\mathcal{U}^h\subset\mathcal{U}$. They read:

$$\begin{aligned}\eta\approx\eta^h&=\sum_{i=1}^{N_V}\eta_i\phi_i,\\ \mathbf{u}\approx\mathbf{u}^h&=\sum_{j=1}^{N_S}\mathbf{u}_j\psi_j,\end{aligned}$$

where η_i and $\mathbf{u}_j$ represent elevation and velocity nodal values, and ϕ_i and ψ_j represent the elevation and velocity shape functions associated with a particular node. The nodal values are then computed by using the Galerkin procedure which amounts to replacing $\hat{\eta}$ by ϕ_i and $\hat{\mathbf{u}}$ by $(\psi_j,0)$ and $(0,\psi_j)$ in equations (7) and (8) respectively, for $1\le i\le N_V$ and $1\le j\le N_S$.

4 The non-conforming mixed $P_1^{NC}-P_1$ discretization

In this study, the elevation and velocity variables are approximated by linear conforming (P_1) and linear non-conforming (P_1^{NC}) shape functions respectively (Fig. 1). Elevation nodes are thus lying on the vertices of the triangulation and velocity nodes are located at mid-segments. With this choice of shape functions, the discrete elevation field is continuous everywhere whereas the discrete velocity field is only continuous across triangle boundaries at mid-side nodes and discontinuous everywhere else around a triangle boundary. A major advantage of non-conforming shape functions is their orthogonality property:

$$\int_\Omega\psi_p\psi_q\ \mathrm{d}\Omega=\frac{A_q}{3}\delta_{pq},$$

where A_q is the area of the support of ψ_q, and δ_{pq} is the Kronecker delta. Such an unusual property increases the computational efficiency of the numerical model. Like the elevation, the depth h is discretized with linear conforming shape functions.

To improve the efficiency of the scheme, it may appear natural to perform the following approximation in the variational formulation (7)-(8):

$$\underbrace{\int_{\Gamma_l} \langle (h+\eta)\mathbf{u}\cdot\mathbf{n}\rangle[\phi_i]\ \mathrm{d}\Gamma}_{=0} + \int_{\Gamma_l} [(h+\eta^h)\mathbf{u}^h\cdot\mathbf{n}]\langle\phi_i\rangle\ \mathrm{d}\Gamma \simeq 0. \tag{9}$$

As P_1 shape functions are continuous, the jump of the elevation shape function vanishes and the first term in (9) is exactly equal to zero. The second term is neglected in order to enforce mass conservation. Indeed, the thickness flux is discontinuous between triangles and neglecting the second integral amounts to weakly impose its continuity. As a result, mass conservation is guaranteed at the cost of a small loss of accuracy.

A second approximation in the formulation (7)-(8) amounts to use a global linear approximation for the product of $\mathbf{u}^h$ with f:

$$\begin{aligned}\int_{\Omega_e} f(\mathbf{k}\times\mathbf{u}^h)\psi_j\ \mathrm{d}\Omega &= \int_{\Omega_e} f\sum_{i=1}^{N_S}(\mathbf{k}\times\mathbf{u}_i)\psi_i\psi_j\ \mathrm{d}\Omega\\ &\simeq \int_{\Omega_e} \underbrace{\sum_{i=1}^{N_S} f_i(\mathbf{k}\times\mathbf{u}_i)\psi_i}_{(f\mathbf{k}\times\mathbf{u})^h}\psi_j\ \mathrm{d}\Omega,\end{aligned} \tag{10}$$

where f_j represent the value of the Coriolis parameter at a velocity node. Equation (10) greatly simplifies the algebra and has a small impact on the accuracy of the solution since f varies very smoothly.

To summarize, the space discretized equations for the Eulerian formulation simply read:

$$\sum_{e=1}^{N_E}\int_{\Omega_e}\left(\frac{\partial\eta^h}{\partial t}\phi_i - (h+\eta^h)\mathbf{u}^h\cdot\boldsymbol{\nabla}\phi_i\right)\mathrm{d}\Omega = 0 \quad \text{for } 1\le i\le N_V, \tag{11}$$

$$\sum_{e=1}^{N_E}\int_{\Omega_e}\left(\frac{\partial\mathbf{u}^h}{\partial t}\psi_j - \mathbf{u}^h\boldsymbol{\nabla}\cdot(\mathbf{u}^h\psi_j) + (f\mathbf{k}\times\mathbf{u})^h\psi_j + g\boldsymbol{\nabla}\eta^h\psi_j\right)\mathrm{d}\Omega$$

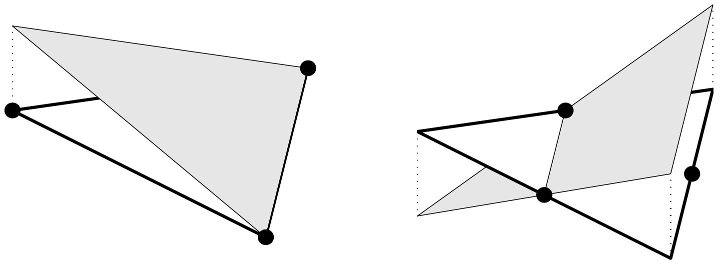

Figure 1. Linear conforming (left) and non-conforming (right) shape functions.

$$+\sum_{l=1}^{N_\Gamma}\int_{\Gamma_l}\langle\mathbf{u}^h\mathbf{u}^h\cdot\mathbf{n}\rangle_\lambda[\psi_j]\ \mathrm{d}\Gamma=0\quad\text{for } 1\le j\le N_S. \tag{12}$$

The last boundary term can be interpreted as follows. Weak continuity of the normal flow through the segment Γ_l between adjacent elements Ω_e and Ω_f is imposed in the usual way of the Discontinuous Galerkin formulation. For a so-called fully upwind scheme ($\lambda = \frac{1}{2}\mathrm{sign}(\mathbf{u}\cdot\mathbf{n})$), the continuity is enforced as a weak inlet boundary condition for Ω_e if the characteristics that go through Γ_l are going in Ω_e. This is fully in line with the mathematical theory of hyperbolic partial differential equations and the presentation of the Discontinuous Galerkin formulation in the pioneering paper of Le Saint and Raviart (1974).

The proposed Eulerian formulation strictly conserves mass but does not exactly conserve the total energy of the flow. The formulation appropriate for semi-Lagrangian time stepping can be obtained by applying the same spatial discretization procedure to equations (3) and (4).

5 Eulerian scheme

To obtain an Eulerian discretization of the nonlinear shallow water equations, (11) and (12) still need to be discretized in time. In order to simplify the notations, we present the temporal discretization of (1) and (2). So, for a given time step $\Delta t = t^{n+1} - t^n$, we obtain:

$$\begin{aligned}\frac{\mathbf{u}^{n+1}-\mathbf{u}^n}{\Delta t}+\mathbf{u}^n\cdot\boldsymbol{\nabla}\mathbf{u}^n+f\mathbf{k}\times\Big(\beta\mathbf{u}^{n+1}+(1-\beta)\mathbf{u}^n\Big)&\\ +g\Big(\alpha\boldsymbol{\nabla}\eta^{n+1}+(1-\alpha)\boldsymbol{\nabla}\eta^n\Big)&=0,\end{aligned} \tag{13}$$

$$\frac{\eta^{n+1}-\eta^{n-1}}{2\Delta t}+\boldsymbol{\nabla}\cdot\Big(\gamma h\mathbf{u}^{n+1}+(1-\gamma)h\mathbf{u}^{n-1}\Big)+\boldsymbol{\nabla}\cdot(\eta^n\mathbf{u}^n)=0, \tag{14}$$

where α, β and γ are implicity coefficients in $[0,1]$ used to vary the time centering of the gradient, Coriolis and divergence terms respectively.

In equations (13) and (14), all linear terms are discretized with a so-called θ-scheme and the nonlinear terms are treated explicitly. In such an approach, the most constraining terms (i.e. those responsible for the propagation of inertia-gravity waves) can be treated implicitly. In particular, the Coriolis term is always discretized semi-implicitly. The value of the other parameters is problem dependent and is given below where numerical experiments are described. A leap frog time scheme is used in equation (14) to discretize the term $\boldsymbol{\nabla}\cdot(\eta^n\mathbf{u}^n)$. Indeed, the scheme would be unconditionnally unstable if an Euler scheme was used instead. However, when the surface-elevation is small compared to the depth of the fluid, i.e. $\eta \ll h$, the term $\boldsymbol{\nabla}\cdot(\eta^n\mathbf{u}^n)$ may be neglected in (14) and an Euler scheme can then be used in the mass equation. The divergence term $\boldsymbol{\nabla}\cdot(h\mathbf{u})$ is then discretized at time steps $n+1$ and n instead of $n+1$ and $n-1$. It should be noted that treating the nonlinear terms explicitly, does not lead to very constraining stability conditions for large scale applications. However, for applications that require high resolution, it may be penalizing.

After replacing η^h and $\mathbf{u}^h$ by their expression in terms of the nodal values in equations (11) and (12) and applying the temporal discretization described above, the following set of linear equations is obtained:

$$\begin{pmatrix} \mathsf{B_{UU}} & \mathsf{G_{UH}} \\ -\mathsf{D_{HU}} & \mathsf{M_{HH}} \end{pmatrix} \begin{pmatrix} \mathsf{U}^{n+1} \\ \mathsf{H}^{n+1} \end{pmatrix} = \begin{pmatrix} \mathsf{R_U} \\ \mathsf{R_H} \end{pmatrix}, \tag{15}$$

where U^{n+1} and H^{n+1} are the nodal values vectors, defined as:

$$\mathsf{U}^{n+1} = \begin{pmatrix} u_i \\ v_i \end{pmatrix} \text{ and } \mathsf{H}^{n+1} = \begin{pmatrix} \eta_j \end{pmatrix},$$

with $1 \leq i \leq N_S$ and $1 \leq j \leq N_V$. The matrix in the left hand side (lhs) of (15) and the vector in the right hand side (rhs) of (15) are explicitly written in the Appendix.

Thanks to the orthogonality of linear non-conforming shape functions, the matrix $\mathsf{B_{UU}}$ is composed of four diagonal sub-matrices. Its inverse can thus be easily computed. The solution vector for the velocity is expressed from (15) as:

$$\mathsf{U}^{n+1} = -\mathsf{B_{UU}^{-1}}\mathsf{G_{UH}}\mathsf{H}^{n+1} + \mathsf{B_{UU}^{-1}}\mathsf{R_U}, \tag{16}$$

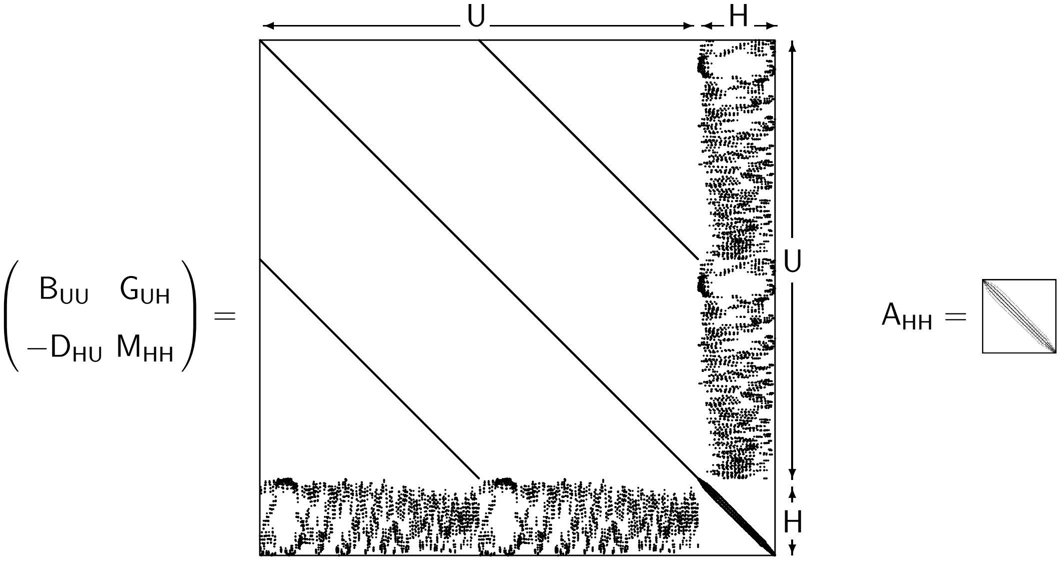

Figure 2. Sparcity patterns of the system matrix before (left) and after (right) the substitution procedure. Both matrices are represented on the same scale.

and then substituted in the mass balance equation, to give:

$$\underbrace{\left(\mathsf{M_{HH}} + \mathsf{D_{HU}}\mathsf{B_{UU}^{-1}}\mathsf{G_{UH}}\right)}_{\equiv\, \mathsf{A_{HH}}} \mathsf{H}^{n+1} = \mathsf{R_H} + \mathsf{D_{HU}}\mathsf{B_{UU}^{-1}}\mathsf{R_U}, \tag{17}$$

where the matrix $\mathsf{A_{HH}}$ is a sparse matrix (as shown in Fig. 2) having an average of 13 non-zero entries per line.

A linear solver is only required to solve equation (17). Once the elevation nodal values are obtained, the velocity nodal values are computed explicitly from (16). The substitution greatly reduces the computational cost as we solve a system of only N_V equations instead of $2N_S + N_V$, i.e. approximately $7N_V$ equations. Fig. 2 shows the sparcity patterns of the initial and final system of equations. Both matrices are represented on the same scale. A generalized minimal residual iterative solver (Saad and Schultz, 1986) has been selected as $\mathsf{A_{HH}}$ is a nonsymmetric matrix in view of the Coriolis term.

6 Semi-Lagrangian scheme

In the semi-Lagrangian method, total derivatives are treated as time differences along particles trajectories while preserving the gridpoint nature of Eulerian schemes. This is achieved by selecting a specific set of fluid parcels at each time step and requiring that they arrive at mesh nodes at the end of the time step. Therefore, the total derivative of a function f is simply the value of f at the arrival point (a mesh node) minus the value of f at the departure point (usually not a mesh node), divided by Δt. By tracking back fluid parcels in time, it is possible to locate their upstream positions at previous time steps. An interpolation formula is then needed to determine the upstream value of the advected quantity at the departure points.

The temporal discretization used for the semi-Lagrangian scheme reads:

$$\frac{\mathbf{u}^{n+1}-\mathbf{u}_d^n}{\Delta t}+f\mathbf{k}\times\Big(\beta\mathbf{u}^{n+1}+(1-\beta)\mathbf{u}_d^n\Big)$$
$$+g\Big(\alpha\boldsymbol{\nabla}\eta^{n+1}+(1-\alpha)\boldsymbol{\nabla}\eta_d^n\Big)=0, \qquad (18)$$

$$\frac{\Big(\ln(h+\eta)\Big)^{n+1}-\Big(\ln(h+\eta)\Big)_d^n}{\Delta t}+\boldsymbol{\nabla}\cdot\Big(\gamma\mathbf{u}^{n+1}+(1-\gamma)\mathbf{u}_d^n\Big)=0, \qquad (19)$$

where the subscript d denotes the evaluation at the departure point and the absence of subscript denotes evaluation at the arrival point. The coefficients α, β and γ are defined as in the Eulerian case. It should be noted that semi-Lagrangian discretizations generally allow the use of larger time steps than Eulerian discretizations.

As for the Eulerian scheme, we substitute $\mathbf{u}$ in terms of η in the continuity equation at the discrete level. Since equation (19) is weakly nonlinear due to the logarithm, a Newton's procedure has to be used to linearized it. An Helmholtz equation for the elevation is then produced.

6.1 Calculation of total derivatives

The semi-Lagrangian procedure requires to evaluate the departure points of the fluid parcels. If $(\mathbf{x}_m, t+\Delta t)$ denotes the arrival point of a fluid parcel, its departure point is then $(\mathbf{x}_m-\mathbf{d}_m, t)$. The displacement of the parcel, $\mathbf{d}_m$, is obtained from a number of iterations (usually two) of a second-order mid-point Runge-Kutta corrector:

$$\mathbf{d}_m^{(k+1)}=\Delta t\ \mathbf{u}(\mathbf{x}-\mathbf{d}_m^{(k)}/2, t+\Delta t/2), \qquad (20)$$

with a first order estimate $\mathbf{d}_m^{(0)}=\Delta t\ \mathbf{u}(\mathbf{x},t)$. This amounts to approximate the exact trajectory of the fluid parcel by a straight line (Fig. 3). The velocity at time $t+\frac{\Delta t}{2}$ in (20) is found by extrapolating the velocity field at time t and $t-\Delta t$, using a two time level scheme (Temperton and Staniforth, 1987; McDonald and Bates, 1987) and yielding an $O(\Delta t^2)$-accurate estimate. When iteratively solving (20), interpolation is required to compute the velocity between mesh

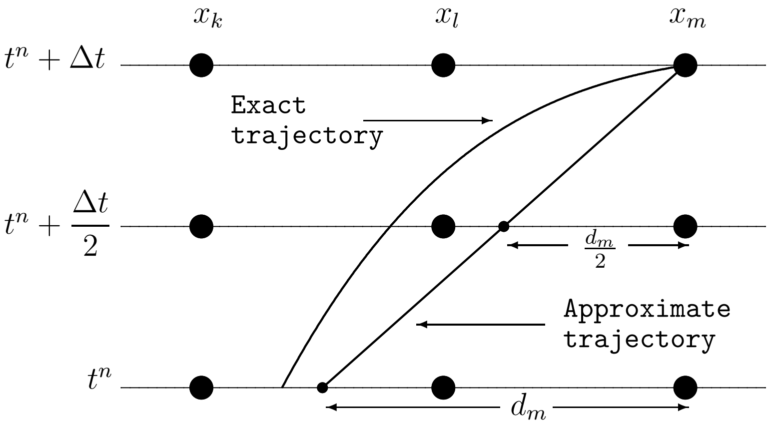

Figure 3. A two-time-level semi-Lagrangian advection scheme. Approximate and exact trajectories arrive at node x_m at time $t^n + \Delta t$. Here, d_m is the displacement of the particle in the x-direction in time Δt.

points. As observed by Staniforth and Côté (1990), negligibly small differences in the solution result from using linear rather than cubic interpolation while solving equation (20). Hence linear interpolation is adopted here.

Once the departure points are computed, the advected variables have to be evaluated at those points. As they usually do not lie on mesh nodes, some form of interpolation is needed. The choice of the interpolator has a crucial impact on the accuracy of the method. In regular domains with structured meshes, various polynomial interpolation schemes have been tried, including linear, quadratic, cubic and quintic Lagrange polynomials, and bicubic splines. McCalpin (1988) showed that low order interpolations can have a very diffusive effect. As a result, semi-Lagrangian models of the atmosphere are usually build with high order interpolations. Among those, bicubic spline interpolations are found to be a good compromise between accuracy and computational cost (Purnell, 1976; Pudykiewicz and Staniforth, 1984).

However, most of atmospheric models are based on orthogonal grids, made up of quadrilaterals. It is found that when the mesh loses its orthogonality, the bicubic spline interpolation is much less accurate. Since we intend to interpolate on an unstructured ocean mesh, another method is needed and interpolation schemes that do not depend on the geometry should be prefered. Le Roux et al. (1997) suggested to use a kriging scheme.

6.2 Kriging interpolation

The term "kriging" has been introduced by Matheron (1973) to honor the pioneering work of Krige (1951). A kriging interpolator can be defined as the best linear unbiased estimator of a random function. It yields equally favourable results for structured and unstructured meshes. Given a serie of N measurements f_i of a function f at different locations $\mathbf{x}_i$ ($1 \leq i \leq N$), kriging constructs an approximate function f^h expressed as the sum of a drift $a(\mathbf{x})$ and a fluctuation $b(\mathbf{x})$:

$$f(\mathbf{x}) \approx f^h(\mathbf{x}) = a(\mathbf{x}) + b(\mathbf{x}).$$

The drift is generally a polynomial which follows the physical phenomenon and the fluctuation is adjusted so that the interpolation fits the data points exactly.

For the sake of simplicity, we illustrate kriging by constructing the approximate function in the one dimensional case, using a linear drift:

$$\begin{aligned} f^h(x) &= a(x) + b(x), \\ &= a_1 + a_2 x + \sum_{j=1}^{N} b_j K(|x - x_j|), \end{aligned}$$

where the function K, known as the generalized covariance, fixes the degree of the fluctuation. The coefficients a_1, a_2, b_1, ..., b_N are calculated by requiring that: (1) the interpolation has no bias, (2) the squared variance of the fluctuation is minimal and (3) the interpolation fits the data points exactly (Trochu, 1993). Those constraints read:

$$\sum_{j=1}^{N} b_j = 0, \quad \sum_{j=1}^{N} b_j x_j = 0 \quad \text{and} \quad f^h(x_i) = f(x_i) \quad \text{for } 1 \leq i \leq N.$$

Hence, the following linear system, known as the dual linear kriging system, is obtained:

$$\left(\begin{array}{ccc|cc} & & & 1 & x_1 \\ & K_{ij} & & \vdots & \vdots \\ & & & 1 & x_N \\ \hline 1 & \ldots & 1 & 0 & 0 \\ x_1 & \ldots & x_N & 0 & 0 \end{array}\right) \left(\begin{array}{c} b_1 \\ \vdots \\ b_N \\ \hline a_1 \\ a_2 \end{array}\right) = \left(\begin{array}{c} f(x_1) \\ \vdots \\ f(x_N) \\ \hline 0 \\ 0 \end{array}\right), \tag{21}$$

where $K_{ij} = K(|x_i - x_j|)$. The matrix of the linear system is a full matrix with zeros on the diagonal. As it only depends on mesh node positions, a LU decomposition needs only to be performed once. Nevertheless, each interpolation requires the resolution of a linear system. The computational cost can thus be significant, especially for problems with large data sets. The final system of discrete shallow water equations is still solved with a GMRES iterative solver.

The accuracy of the kriging interpolation method is determined by a suitable choice of the drift and the fluctuation. The drift is usually a low order polynomial. The choice of an admissible generalized covariance has been discussed by Matheron (1980) and Christakos (1984) and the most employed are $K(h) = -h$, $K(h) = h^2 \ln h$ and $K(h) = h^3$, with $h = |x_i - x_j|$, for $1 \leq i, j \leq N$.

7 Numerical simulations and discussions

In this section, we perform some experiments to assess the different numerical models introduced previously. As a test problem, we consider the propagation of slow Rossby waves. Despite the fact that they are very slow, Rossby waves have a major effect on the large scale circulation, and thus on weather and climate. For instance, Rossby waves can intensify western boundary currents, as well as push them off their usual course. As those currents transport huge quantities of heat, it is readily understood that even a minor shift in the position of the current can dramatically affect weather over large areas of the globe. Those waves can be represented with the shallow water equations.

The two numerical tests used in (Le Roux et al., 2000) are reproduced here with the $P_1^{NC} - P_1$ pair in the Eulerian and semi-Lagrangian approaches. For both tests, the model is run as a reduced gravity model with parameters set to correspond to the first internal vertical mode of a baroclinic model. A second passive layer is implicitly assumed infinitely deep and at rest. The depth of the fluid h is set constant.

7.1 Equatorial Rossby soliton

We first reproduce the propagation of the equatorial Rossby soliton of Boyd (1980). This experiment has also been performed by Iskandarani et al. (1995) with their spectral element shallow water model. The model equations are rewritten in their dimensionless form on an equatorial β plane. Dimensionless variables read: $\mathbf{x}' = \mathbf{x}/L$, $t' = t/T$, $\mathbf{u}' = \mathbf{u}/U$ and $\eta' = \eta/h$. The characteristic length (L), time (T) and velocity (U) scales are expressed in terms of the Lamb parameter E:

$$L = \frac{a}{E^{1/4}}, \quad T = \frac{E^{1/4}}{2\Omega}, \quad U = \sqrt{g'h}, \quad E = \frac{4\Omega^2 a^2}{g'h},$$

where a is the radius of the Earth and Ω denotes here the angular frequency of the Earth rotation. The reduced gravity and mean depth are taken as $g' = 4 \times 10^{-2}$ ms^{-2} and $h = 100$ m respectively. The mean gravity wave speed is then $U = 2$ ms^{-1} and it corresponds to the wave speed of the first baroclinic mode. Those values yield a time scale of 41 h and a length scale of 296 km.

The rectangular domain non-dimensional extent is 32×8. The mesh is unstructured and its resolution goes from 0.5 to 1 non-dimensional unit (Fig. 4a). There are 1768 elements and 946 nodes. The temporal discretization is semi-implicit ($\alpha = \beta = \gamma = 1/2$) and the non-dimensional time step is set to 0.25. As intial conditions, we use the zeroth-order solution introduced by Boyd (1980) at time $t' = 0$. This solution reads:

$$
\begin{aligned}
u'(x',y',t') &= AB^2\frac{(6y'^2-9)}{4}\ \mathrm{sech}^2\left(B(x'-ct')\right)\ \exp(-y'^2/2),\\
v'(x',y',t') &= -4AB^3y'\ \tanh\left(B(x'-ct')\right)\ \mathrm{sech}^2\left(B(x'-ct')\right)\ \exp(-y'^2/2),\\
\eta'(x',y',t') &= AB^2\frac{(6y'^2+3)}{4}\ \mathrm{sech}^2\left(B(x'-ct')\right)\ \exp(-y'^2/2),
\end{aligned}
$$

where $A = 0.771$ and $B = 0.395$. The non-dimensional, linear, non-dispersive velocity phase speed is $c = -\frac{1}{3} - 0.395B^2$. The initial elevation field is shown in Fig. 4b. It should be noted that Boyd (1985) gives a first order solution to the Rossby soliton problem. This solution is however not considered in this work.

At the beginning of the integration, the soliton loses approximately 5% of its amplitude which propagates eastward as equatorial Kelvin waves. This is due to the initial condition that is not exactly a solitary wave. Meanwhile, the soliton propagates westward with little change in shape and amplitude, in agreement with the theory. The elevation field after 32 non-dimensional time units is shown in Fig. 5 for the Eulerian scheme and the semi-Lagrangian method. The asymptotic solution of Boyd (1980) is also given. The semi-Lagrangian approach is based on linear and kriging interpolation schemes. The latter use the following generalized covariance functions: $-h$, $h^2\ln(h)$, h^3 and $-h^5$. The Eulerian scheme preserves the shape of the soliton quite well with moderate damping. It gives a phase speed of 0.783 ms^{-1} which is in good agreement with the asymptotic solution of Boyd (1980) that predicts a value of 0.79 ms^{-1}. The semi-Lagrangian models provide a phase speed ranging from 0.78 to 0.83 ms^{-1} for Lagrangian linear and the various kriging interpolations. It is observed that the phase speed increases with the order of the interpolation used. As expected, the semi-Lagrangian method using low order interpolating schemes shows more damping. As the order of the interpolation increases, the solution gets better. However, for high order interpolations, there is very little numerical diffusion and instabilities may arise. This is observable in Fig. 5 for the kriging scheme with $K(h) = -h^5$.

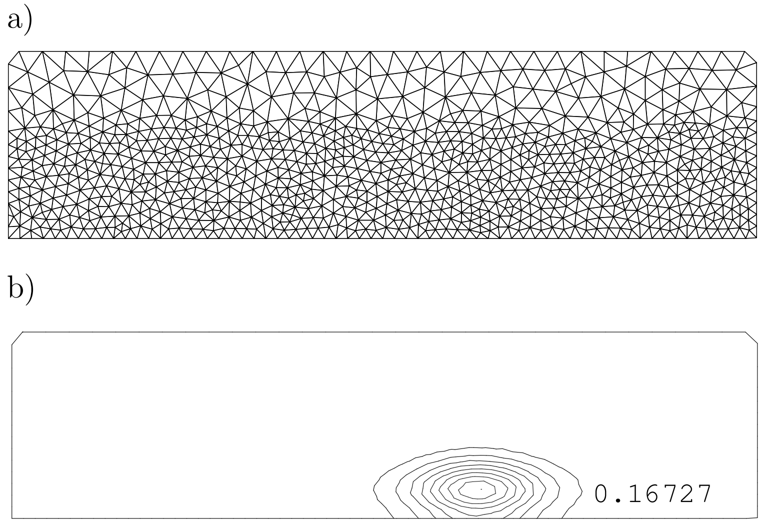

Figure 4. (a) Mesh used in the equatorial Rossby soliton experiment. (b) Isolines of the elevation field at initial time, the non-dimensional maximum value is specified in the bottom-right corner. There are 10 isolines at equidistributed values ranging form zero to the maximum value specified.

7.2 Eddy propagation in the Gulf of Mexico

In the second experiment, the slowly propagating Rossby modes are simulated in the case of the evolution of a typical anticyclonic eddy at midlatitudes. The Gulf of Mexico is chosen as the domain to test the model in a realistic geometry. In the present simulation, we ignore the inflow and outflow through the Yucatan Channel and Florida Straits and the basin is assumed closed. Although this experiment is highly idealized, it is expected to represent some of the features of the life cycle of anticyclonic eddies in the Western part of the Gulf. The experiment focuses mainly on the westward propagation of the eddies and their interaction with the boundary. This is why the unstructured mesh, shown in Fig. 6, has a higher resolution in the western part of the domain. There are 8001 elements and 4092 nodes. The domain extent is approximately 1800 km × 1350 km and the resolution of the mesh goes from 20 to 60 km.

A Gaussian distribution of η, centered at the origin of the domain, is prescribed at initial time:

$$\eta(x, y, 0) = C \exp[-D(x^2 + y^2)],$$

where $C = 68.2$ m and $D = 5.92 \times 10^{-11}$ m^{-2}. The β-plane assumption is made (i.e. $f = f_0 + \beta y$) and f_0 and β are evaluated at 25°N. The reduced

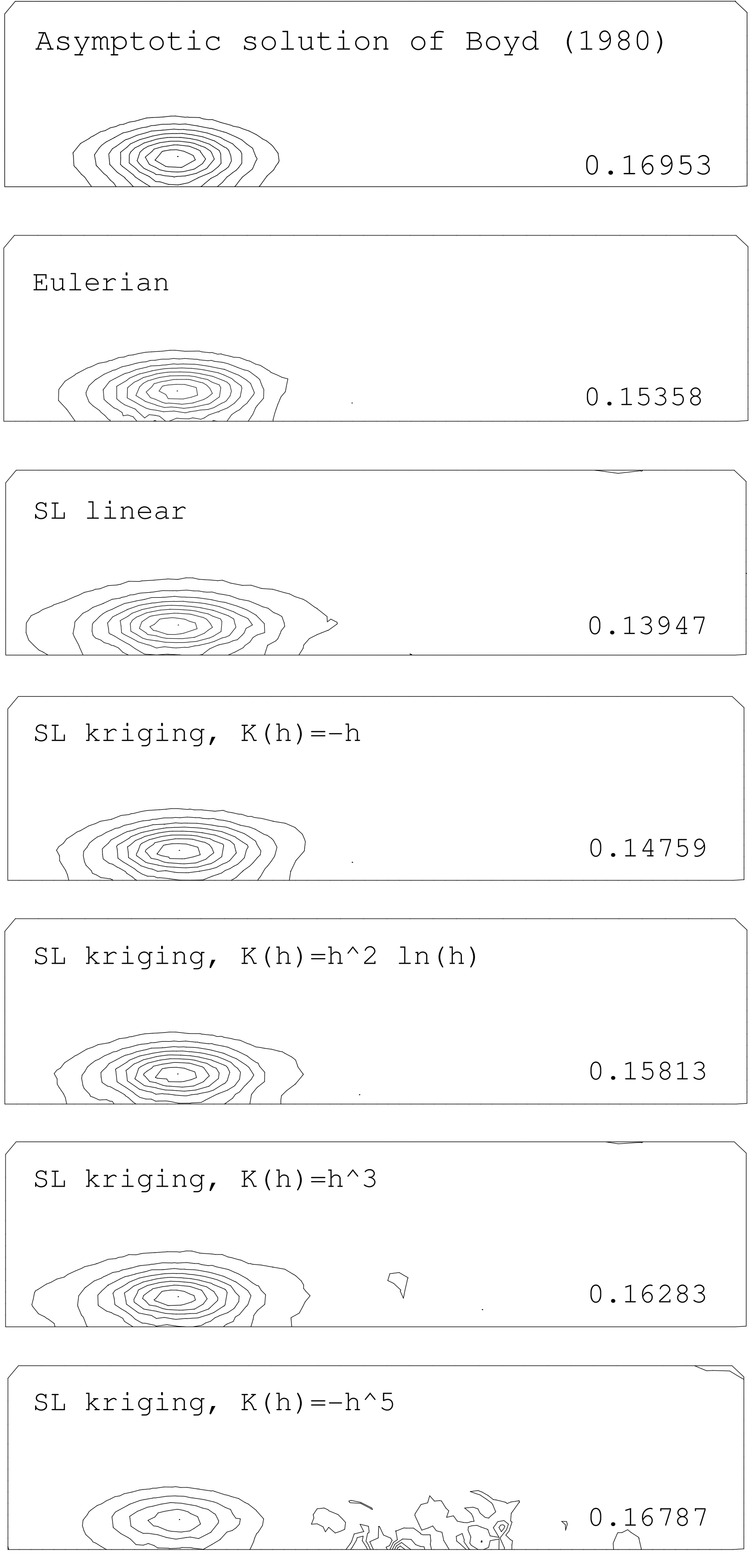

Figure 5. Elevation fields after 55 days ($t = 32\ T$) obtained from the asymptotic relation, the Eulerian scheme and various the semi-Lagrangian schemes. The non-dimensional maximum value is specified at the bottom-right corner of each panel. The number of isolines is the same as in Fig. 4.

gravity and mean depth are taken as $g' = 1.37 \times 10^{-1}$ ms^{-2} and $h = 100$ m, respectively, so that the mean gravity wave speed is $c \equiv \sqrt{g'h} \approx 3.7$ ms^{-1}. The radius of deformation at midbasin is thus $R_d \equiv c/f_0 \approx 6 \times 10^4$ m. The initial velocity field is taken to be in geostrophic balance and so

$$u(x,y,0) = 2\frac{g'}{f}CDy\exp[-D(x^2+y^2)],$$
$$v(x,y,0) = -2\frac{g'}{f}CDx\exp[-D(x^2+y^2)].$$

By setting $C = 68.2$ m, the maximum flow speed is 1 ms^{-1}. The parameters values are chosen to match the observations of the eddies made by Lewis and Kirwan (1987). In (13) and (14), the temporal discretization is now explicit for the divergence term, and semi-implicit for Coriolis and the gradient terms ($\alpha = \beta = 1/2$, $\gamma = 0$). The time step is set to 300 s, hence the gravitational Courant number is close to 0.1.

In this experiment, we consider the Eulerian scheme and the semi-Lagrangian method using Lagrangian linear and kriging (with $K(h) = h^3$) interpolation schemes. The Lagrangian linear interpolation is chosen to illustrate the poor results obtained with low order interpolations. The kriging scheme with $K(h) = h^3$ is selected as it appeared to give good results for the soliton experiment, with very small damping. This interplation scheme is equivalent to cubic spline interpolation (Le Roux et al., 1997).

The semi-Lagrangian method using the kriging scheme develop some small-amplitude noise in the velocity field, which progressively amplified as the integration progressed and ultimately led to unacceptable results. As most high order schemes, such an approach exhibiting better accuracy is more sensitive to errors accumulation. Some harmonic diffusion was therefore introduced for velocity. At the end of each time step, a diffusive correction is applied to the provisional velocity field computed from the semi-Lagrangian scheme, denoted $\mathbf{u}^*$. The corrected velocity field, $\mathbf{u}$, is then obtained by solving:

$$\frac{\mathbf{u} - \mathbf{u}^*}{\Delta t} = \nu \nabla^2 \mathbf{u}^*,$$

subject to zero-flux boundary conditions, where ν is the diffusion coefficient. A value of $\nu = 175$ m^2 s^{-1} was found sufficient to suppress the noise in the velocity field.

At initial time, the eddy is located in the middle of the Gulf of Mexico (Fig. 7) and different stages of its propagation are shown in Fig. 8 and Fig. 9 for the Eulerian and the semi-Lagrangian models. Shortly after initialization, there is a readjustment of the flow and η loses approximately 10% of its amplitude.

Afterward, the Rossby wave propagates westward with a slight southwesterly drift that is due to nonlinear effects. The reduction in amplitude that follows the readjustment is due to the explicit and/or implicit diffusion in the numerical schemes. The implicit diffusion is due to the upwind treatment of momentum advection for the Eulerian scheme, and to the interpolation procedure for the semi-Lagrangian schemes. The Eulerian and the high order semi-Lagrangian schemes qualitatively give comparable results. For both schemes, the translation speed is approximately 6.8 km day^{-1} which is in good agreement with that predicted by the theory ($\beta R_d^2 = 6.5$ km day^{-1}). The linear semi-Lagrangian schemes shows more dispersion and gives a slower propagation speed. The maximum values of the elevation and flow-speed fields show that the semi-Lagrangian scheme using a linear interpolation is very diffusive as the eddy loses approximately 70% of its amplitude compared to the Eulerian scheme during the simulation. This is due to the low order interpolation procedure. The high order semi-Lagrangian scheme performs better but the viscosity required to avoid instabilities leads to a 8% reduction in η compared to the Eulerian scheme, after 11 weeks of simulation.

The Eulerian scheme is stable enough to run without explicit diffusion whereas the high order semi-Lagrangian scheme requires some explicit diffusion to run properly. The stability of the Eulerian scheme is partly due to the upwind treatment of momentum advection which has a diffusive effect. We estimate the amount of artificial diffusion in the Eulerian scheme by running that model with an explicit diffusion $\nu = 175$ ms^{-2}. By comparing the results of the Eulerian and high order semi-Lagrangian model when both use the same explicit diffusion, it is possible to estimate the effect of the artificial diffusion "hidden" in the Eulerian model. The high order semi-Lagrangian model is assumed to have a very small implicit diffusion. The final elevation fields obtained with the inviscid Eulerian, the viscous Eulerian and the viscous kriging semi-Lagrangian schemes are shown in Fig. 10. It can be seen that the results obtained with the viscous Eulerian scheme are very close to those obtained with the viscous kriging semi-Lagrangian scheme. This suggests that the amount a artificial diffusion introduced in the Eulerian scheme by the upwind treatment of momentum advection is very small and has less impact than the explicit diffusion needed to run the high-order semi-Lagrangian scheme.

8 Conclusions

The nonlinear shallow water equations have been discretized on an unstructured triangular grid by using the $P_1^{NC} - P_1$ finite element pair. Eulerian and semi-Lagrangian advection schemes have been compared and assessed in the context of ocean modelling. It has been shown that the Eulerian method gives an accurate representation of the Rossby waves as the amplitude and phase

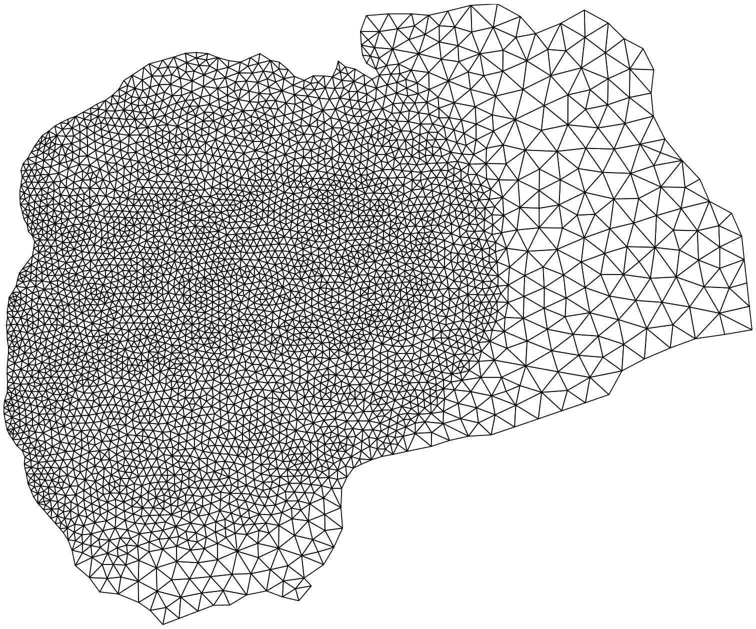

Figure 6. A triangular unstructured mesh of the Gulf of Mexico. The resolution goes from 20 km in the western part to 60 km in the eastern part.

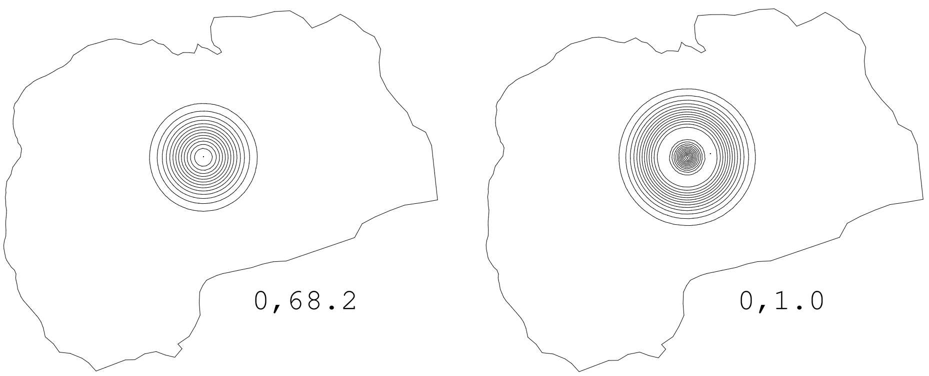

Figure 7. Isolines of the elevation field (bottom-left) and flow-speed field (bottom-right) at initial time. The minimum and maximum values are specified under each figure. For both variables, there are 15 isolines at equidistributed values ranging form the minimum to the maximum values specified (in m and ms^{-1} respectively).

speed of those modes are well preserved during propagation. The method works well without explicit diffusion and the implicit numerical diffusion, mainly due to an upwind momentum advection discretization, seems to have a small impact on the accuracy of the results.

Semi-Lagrangian schemes well reproduce Rossby waves when a high order kriging interpolation is used. Indeed, a high order accuracy is then reached

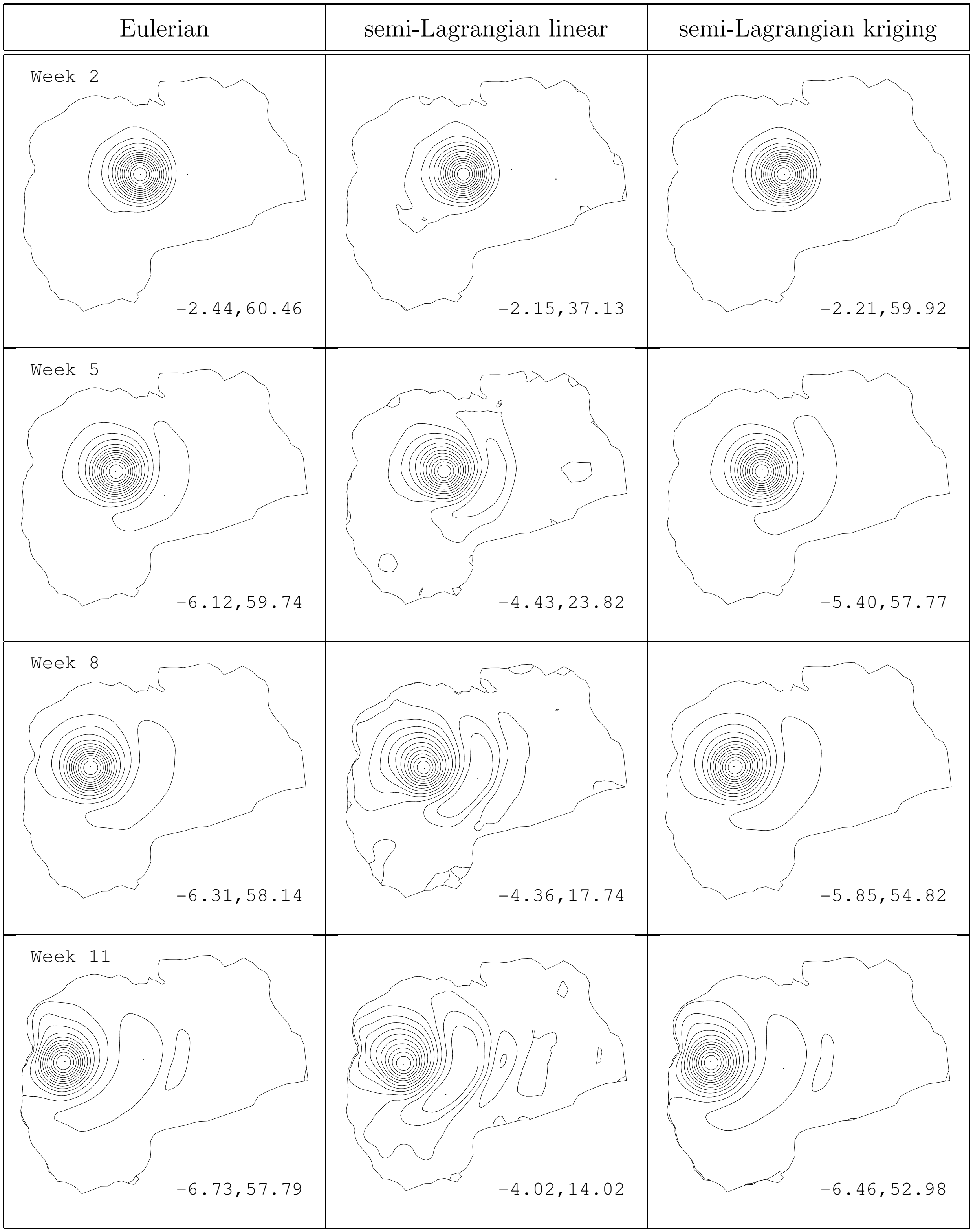

Figure 8. Isolines of the elevation field at different times of the propagation for the Eulerian, semi-Lagrangian with linear interpolator and semi-Lagrangian with kriging interpolator ($K(h) = h^3$) schemes. The minimum and maximum values (in m) are specified at the bottom right corner of each panel. The number of isolines is the same as in Fig. 7.

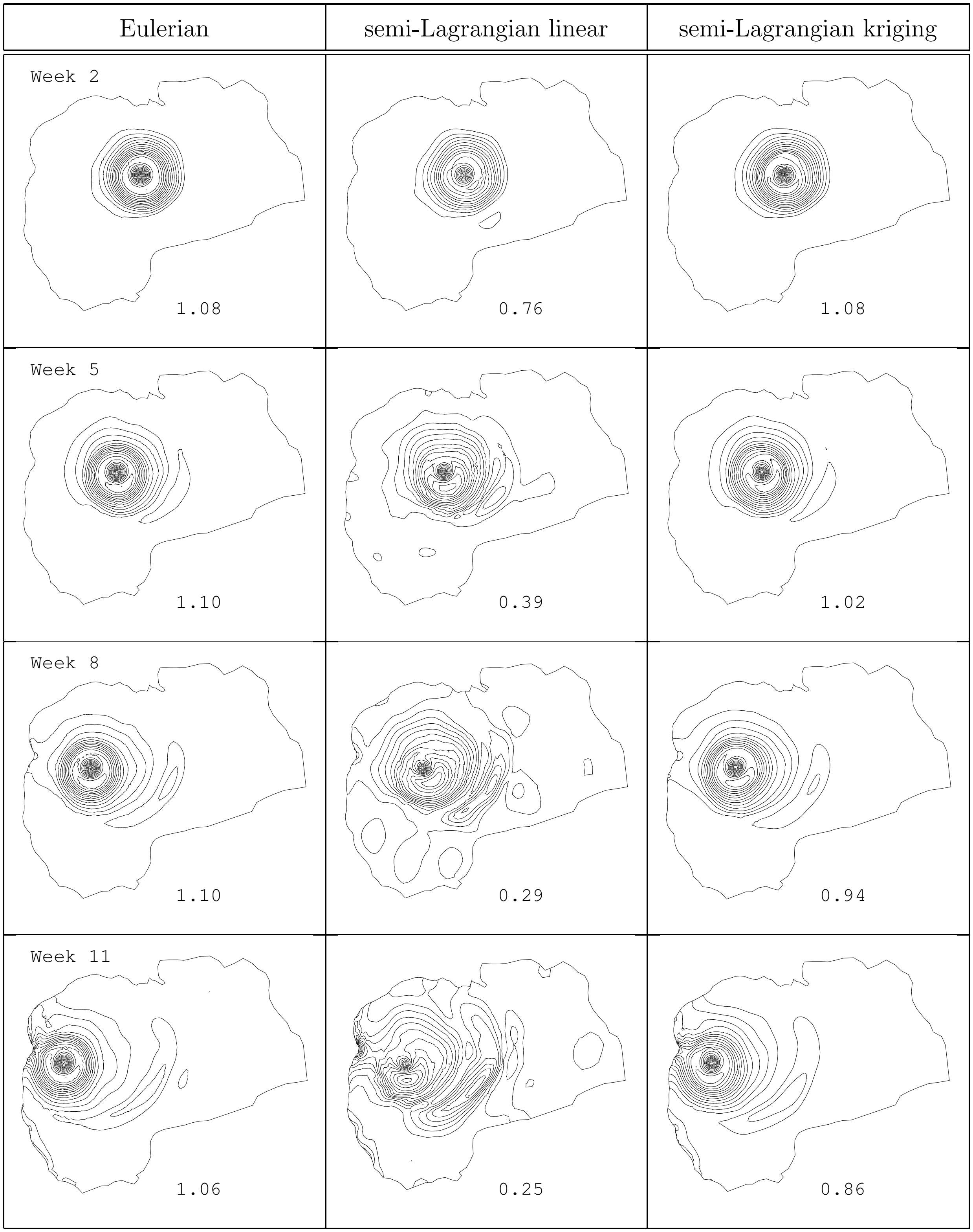

Figure 9. Isolines of the flow-speed field at different times of the propagation for the Eulerian, semi-Lagrangian with linear interpolator and semi-Lagrangian with kriging interpolator ($K(h) = h^3$) schemes. The minimum and maximum values (in ms^{-1}) are specified at the bottom right corner of each panel. The number of isolines is the same as in Fig. 7.

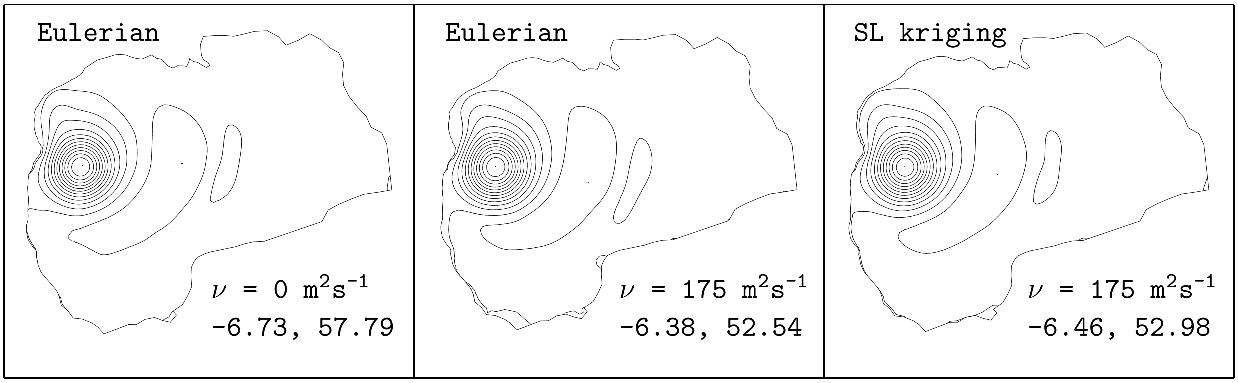

Figure 10. Isolines of the elevation field after 11 weeks for the inviscid Eulerian scheme, and for the Eulerian and kriging semi-Lagrangian schemes with an explicit diffusion $\nu = 175$ m^{2}s^{-1}. The minimum and maximum values are specified at the bottom right corner of each panel. The number of isolines is the same as in Fig. 7.

even on unstructured grids. However, we were forced to add a small Laplacian diffusion to the model to be able to get an acceptable solution. In other words, numerical diffusion has to be incorporated explicitly when using the high order semi-Lagrangian model. In the Eulerian approach, it is observed that the amount of numerical diffusion introduced by upwinding is quite small in comparison.

The comparison of the computational cost between Eulerian and semi-Lagrangian methods is not straightforward as it depends strongly on the implementation, on some numerical strategies and on the linear solver. In one hand, the main advantage of the semi-Lagrangian method compared to the Eulerian scheme, is the possibility of using larger time steps. However, the use of larger time steps leads to a poorer conditionning of the linear system and the benefit in terms of computational cost is not always as good as expected. Moreover, the interpolation procedure and the tracking calculation requires cumbersome implementation and a high computational cost. In the other hand, the Eulerian approach is quite more easy to implement and seems to be considerably much cheaper in terms of CPU requirements. As implemented in our codes, the semi-Lagrangian calculations are at least ten times more expensive than the Eulerian ones.

The Eulerian $P_1^{NC} - P_1$ model seems to be a promising initial step toward the construction of an ocean general circulation model using unstructured triangular meshes. The $P_1^{NC} - P_1$ finite element pair combines several advantages such as the absence of pressure modes, a reasonable computational cost even compared to traditional finite-difference schemes and the possibility to efficiently perform upwinding while computing momentum advection.

Acknowledgements

Emmanuel Hanert and Eric Deleersnijder are Research fellow and Research associate, respectively, with the Belgian National Fund for Scientific Research (FNRS). The support of the Convention d'Actions de Recherche Concertées ARC 97/02-208 with the Communauté Française de Belgique is gratefully acknowledged. Daniel Y. Le Roux is supported by grants from the Natural Sciences and Engineering Research Council (NSERC) and the Fonds Québécois de la Recherche sur la Nature et les Technologies (FQRNT).

A Details on the matricial form of the discrete equations

The matrix figuring in (15) is written as:

$$\left(\begin{array}{c||c} \mathsf{B}_{\mathsf{UU}} & \mathsf{G}_{\mathsf{UH}} \\ \hline\hline -\mathsf{D}_{\mathsf{HU}} & \mathsf{M}_{\mathsf{HH}} \end{array}\right) = \left(\begin{array}{c|c||c} \displaystyle\sum_e \int_{\Omega_e} \psi_i\psi_j & \displaystyle -\beta\Delta t \sum_e \int_{\Omega_e} \psi_i f_j \psi_j & \displaystyle \alpha g \Delta t \sum_e \int_{\Omega_e} \psi_i \phi_{j,x} \\ \hline \displaystyle \beta\Delta t \sum_e \int_{\Omega_e} \psi_i f_j \psi_j & \displaystyle\sum_e \int_{\Omega_e} \psi_i\psi_j & \displaystyle \alpha g \Delta t \sum_e \int_{\Omega_e} \psi_i \phi_{j,y} \\ \hline\hline \displaystyle -\gamma\Delta t \sum_e \int_{\Omega_e} h\phi_{i,x}\psi_j & \displaystyle -\gamma\Delta t \sum_e \int_{\Omega_e} h\phi_{i,y}\psi_j & \displaystyle\sum_e \int_{\Omega_e} \phi_i\phi_j \end{array}\right).$$

The matrix B_{UU} is composed of the velocity mass matrix and the Coriolis matrix. As non-conforming shape functions are orthogonal, the four sub-matrices in B_{UU} are diagonal and the inverse of B_{UU} may thus be easily computed. The matrices G_{UH} and D_{HU} respectively correspond to the gradient and divergence matrices. If h is constant, the divergence matrix is proportional to the transpose of the gradient matrix. Finally, the matrix M_{HH} is the elevation mass matrix.

The rhs of equation (15) reads:

$$\left(\begin{array}{c}\mathsf{R_U}\\ \hline\hline \mathsf{R_H}\end{array}\right) = \left(\begin{array}{c} \sum\limits_e \int\limits_{\Omega_e} \psi_i u_n^h + \Delta t \sum\limits_e \int\limits_{\Omega_e} \boldsymbol{\nabla}\cdot(\mathbf{u}_n^h\psi_i)u_n^h + \beta\Delta t \sum\limits_e \int\limits_{\Omega_e} \psi_i f v_n^h \\ -\alpha g\Delta t \sum\limits_e \int\limits_{\Omega_e} \psi_i \eta^h_{n,x} - \Delta t \sum\limits_l \int\limits_{\Gamma_l} \langle u_n^h \mathbf{u}_n^h\cdot\mathbf{n}\rangle_\lambda[\psi_i] \\ \hline \sum\limits_e \int\limits_{\Omega_e} \psi_i v_n^h + \Delta t \sum\limits_e \int\limits_{\Omega_e} \boldsymbol{\nabla}\cdot(\mathbf{u}_n^h\psi_i)v_n^h - \beta\Delta t \sum\limits_e \int\limits_{\Omega_e} \psi_i f u_n^h \\ -\alpha g\Delta t \sum\limits_e \int\limits_{\Omega_e} \psi_i \eta^h_{n,y} - \Delta t \sum\limits_l \int\limits_{\Gamma_l} \langle v_n^h \mathbf{u}_n^h\cdot\mathbf{n}\rangle_\lambda[\psi_i] \\ \hline\hline \sum\limits_e \int\limits_{\Omega_e} \phi_i \eta_n^h + \gamma\Delta t \sum\limits_e \int\limits_{\Omega_e} h\mathbf{u}_n^h\cdot\boldsymbol{\nabla}\phi_i + \Delta t \sum\limits_e \int\limits_{\Omega_e} \eta_n^h \mathbf{u}_n^h\cdot\boldsymbol{\nabla}\phi_i \end{array}\right),$$

where $\mathbf{u}_n^h$ denotes the value of $\mathbf{u}^h$ at time step n.

References

Behrens, J., 1998. Atmospheric and ocean modeling with an adaptive finite element solver for the shallow-water equations. Applied Numerical Mathematics 26, 217–226.

Boyd, J.P., 1980. Equatorial solitary waves. Part I: Rossby solitons. Journal of Physical Oceanography 10, 1699–1717.

Boyd, J.P., 1985. Equatorial solitary waves. Part 3: Westward-traveling modons. Journal of Physical Oceanography 15, 46–54.

Casulli, V., Walters, R.A., 2000. An unstructured grid, three-dimensional model based on the shallow water equations. International Journal for Numerical Methods in Fluids 32, 331–348.

Chen, C., Liu, H., Beardsley, R.C., 2003. An unstructured grid, finite-volume, three-dimensional, primitive equations ocean model: Applications to coastal ocean and estuaries. Journal of Atmospheric and Oceanic Technology 20, 159–186.

Christakos, G., 1984. On the problem of permissible covariance and variogram models. Water Ressources Research 20, 251–265.

Crouzeix, M., Raviart, P., 1973. Conforming and nonconforming finite-element methods for solving the stationary Stokes equations. R.A.I.R.O. Analyse Numérique 7, 33–76.

Danilov, S., Kivman, G., Schröter, J., 2004. A finite element ocean model: Principles and evaluation. Ocean Modelling 6, 125–150.

Hanert, E., Le Roux, D.Y., Legat, V., Deleersnijder, E., 2004. Advection schemes for unstructured grid ocean modelling. Ocean Modelling 7, 39–58.

Hanert, E., Legat, V., Deleersnijder, E., 2003. A comparison of three finite elements to solve the linear shallow water equations. Ocean Modelling 5, 17–35.

Houston, P., Schwab, C., Suli, E., 2000. Discontinuous $hp-$finite element methods for advection diffusion problems. Tech. Rep. NA-00/15, Oxford University.

Hua, B.L., Thomasset, F., 1984. A noise-free finite element scheme for the two-layer shallow water equations. Tellus 36A, 157–165.

Iskandarani, M., Haidvogel, D.B., Boyd, J.B., 1995. A staggered spectral element model with application to the oceanic shallow water equations. International Journal for Numerical Methods in Fluids 20, 393–414.

Iskandarani, M., Haidvogel, D.B., Levin, J.C., 2003. A three-dimensional spectral element model for the solution of the hydrostatic primitive equations. Journal of Computational Physics 186, 397–425.

Krige, S.R., 1951. A statistical approach to some basic mine valuation problems on the Witwatersrand. J. Chem. Metall. Min. Soc. S. Afr. 52, 119–139.

Le Provost, C., Bernier, C., Blayo, E., 1994. A comparison of two numerical methods for integrating a quasi-geostrophic multilayer model of ocean circulations: Finite element and finite difference methods. Journal of Computational Physics 110, 341–359.

Le Roux, D.Y., 2003. Analysis of the $P_1^{NC} - P_1$ finite-element pair in shallow-water ocean models. SIAM Journal of Scientific Computing, submitted .

Le Roux, D.Y., Lin, C.A., Staniforth, A., 1997. An accurate interpolating scheme for semi-Lagrangian advection on an unstructured mesh for ocean modelling. Tellus 49A2, 119–138.

Le Roux, D.Y., Staniforth, A., Lin, C.A., 2000. A semi-implicit semi-Lagrangian finite-element shallow-water ocean model. Monthly Weather Review 128, 1384–1401.

Le Saint, P., Raviart, P., 1974. On the finite element method for solving the neutron transport equations. In: de Boor, C. (Ed.), Mathematical Aspects of Finite Elements in Partial Differential Equations. Academic Press, pp. 89–145.

Legrand, S., Legat, V., Deleersnijder, E., 2001. Delaunay mesh generation for an unstructured-grid ocean general circulation model. Ocean Modelling 2, 17–28.

Lewis, J.K., Kirwan, A.D., 1987. Genesis of a Gulf of Mexico ring as determined form kinematic analyses. Journal of Geophysical Research 92, 11727–11740.

Lynch, D.R., Ip, J.T.C., Naimie, C.E., Werner, F.E., 1996. Comprehensive coastal circulation model with application to the Gulf of Maine. Continental Shelf Research 16, 875–906.

Matheron, G., 1973. The intrinsic random functions and their applications. Adv. Appl. Probl. 5, 439–468.

Matheron, G., 1980. Splines et krigeage: leur équivalence formelle. Tech. Rep. N-667, Centre de Géostatistique, Ecole des Mines de Paris, Fontainebleau, France.

McCalpin, J.D., 1988. A quantitative analysis of the dissipation inherent in semi-Lagrangian advection. Monthly Weather Review 116, 2330–2336.

McDonald, A., Bates, J.R., 1987. Improving the estimate of the departure point position in a two-level semi-Lagrangian and semi-implicit scheme. Monthly Weather review 115, 737–739.

Myers, P.G., Weaver, A.J., 1995. A diagnostic barotropic finite-element ocean circulation model. Journal of Atmospheric and Oceanic Technology 12, 511–526.

Nechaev, D., Schröter, J., Yaremchuk, M., 2003. A diagnostic stabilized finite-element ocean circulation model. Ocean Modelling 5, 37–63.

Pudykiewicz, J., Staniforth, A., 1984. Some properties and comparative performances of the semi-Lagrangian method of Robert in the solution of the advection-diffusion equation. Atmosphere-ocean , 283–308.

Purnell, D.K., 1976. Solution of the advective equation by upstream interpolation with a cubic spline. Monthly Weather Review 104, 42–48.

Robert, A., 1981. A stable numerical integration scheme for the primitive meteorological equations. Atmosphere-Ocean 19, 35–46.

Robert, A., 1982. A semi-Lagrangian and semi-implicit numerical integration scheme for the primitive meteorological equations. Japan Meteorological Society 60, 319–325.

Robert, A., Yee, T.L., Ritchie, H., 1985. A semi-Lagrangian and semi-implicit numerical integration scheme for multilevel atmospheric models. Monthly Weather Review 113, 388–394.

Saad, Y., Schultz, M.H., 1986. GMRES: a generalized minimal residual algorithm for solving nonsymmetric linear systems. SIAM Journal on Scientific Computing 7, 856–869.

Staniforth, A.N., Côté, J., 1990. Semi-Lagrangian schemes for atmospheric models - a review. Monthly Weather Review 119, 2206–2223.

Temperton, C., Staniforth, A.N., 1987. An efficient two-time level semi-Lagrangian semi-implicit integration scheme. Quarterly Journal of the Royal Meteorological Society 113, 1025–1039.

Trochu, F., 1993. A contouring program based on dual kriging interpolation. Engineering with Computers 9, 160–177.